Comparative of parallel modified B-Spline interpolation again classic interpolation methods in Particle-Mesh step for Non-Linear Electro-Ion dynamics

G. J. Garnica-Castro* and G. Polupan
Instituto Politécnico Nacional, ESIME Zacatenco, Ciudad de México 07738, México,
**e-mail: ggarnicac1500@alumno.ipn.mx; OrcID: 0009-0006-1568-534X*

O. M. Huerta-Chavez† and R. A. Bernal-Orozco
Instituto Politécnico Nacional, ESIME Ticóman, Ciudad de México 07340, México,
†*e-mail: ohuertac@ipn.mx; OrcID: 0000-0002-2932-2033*

R. Escalante
Unidad de Alta Tecnología, Facultad de Ingeniería,
Universidad Nacional Autónoma de México.

Received 5 September 2025; accepted 5 January 2026

This work presents a comparative study of interpolation schemes for the Particle-Mesh step in Particle-in-Cell (PIC) simulations of nonlinear electron-ion dynamics, emphasizing an OpenMP parallel implementation of a modified cubic B-Spline kernel. The modified B-spline introduces a small, zero-mean perturbation close to the standard cubic B-Spline to mimic microscale fluctuations and mitigate oscillations caused by superparticle clustering. We compare this approach against non-parallel modified B-spline, classical cubic B-Spline, and trilinear (cloud-in-cell) interpolation.

We propose a three-dimensional cubic benchmark with controlled initial conditions (following Brieda) to ensure a fair comparison. The metrics include the number of electrons, the electric field, and the conservation of energy. The classical modified B-Spline consistently attenuates noise and suppresses oscillations relative to the CIC and the standard cubic kernel, while preserving force accuracy and not degrading energy conservation beyond baseline levels. The OpenMP implementation achieves substantial speedups; the per-thread, seedable randomization adds only marginal overhead and maintains parallel scalability. Sensitivity analyzes (perturbation amplitude and random seed) indicate stable behavior and reproducibility.

Overall, the OpenMP-parallel randomized cubic B-Spline provides a favorable trade-off between accuracy, robustness, and performance, making it a practical option for high-fidelity PIC of nonlinear electron-ion plasmas.

Keywords: Particle-in-cell; electron-Ion dynamics; OpenMP; particles simulation; HET.

DOI: https://doi.org/10.31349/RevMexFis.72.041501

1. Introduction

To describe the complex phenomena encountered in electric thrusters requires a deep understanding of plasma dynamics [1,2]. One of the most complex phenomena is the electron dynamics, which could help us to describe phenomena such as secondary electron emission (SEE) that can degrade the performance and lifetime of these devices [3]. We outline two modeling paradigms: the fluid model, typically formulated in the framework of magnetohydrodynamics (MHD) [4-7], and the kinetic models based on the Boltzmann equation [4,5].

We reduce the problem to an electrostatic and collisionless framework of the Vlasov-Poisson system. The Vlasov equation [6] follows from the Boltzmann equation under the collisionless assumption; so the variation of the distribution function due to collisions vanishes by definition [7,8]. Using the approximation, we reduce Maxwell's equations to Poisson's equation, which is self-consistently coupled to the dynamics of the particles.

However, the high dimensionality of the Vlasov-Poisson system, defined in the phase space, renders traditional grid solvers, such as the finite element method (FEM), finite volume method (FVM), and finite difference method (FDM), impractical for many real problems [9]. In practice, two approaches are widely used: the Particle-in-Cell (PIC) [1,10-12] and the Direct Simulation Monte Carlo (DSMC) [13-15]. In the framework of Hall-effect thrusters (HET), PIC is extensively used to describe the transport, instabilities, and wall-interaction physics; nonetheless, key aspects of plasma transport (electron-ion dynamics) remain only "partially" understood [16-18], to say the least.

A limitation of conventional PIC is their numerical noise introduced in the Particle-Mesh step, particularly when using low-order interpolation (*e.g.*, Cloud-in-Cell). Such noise can distort or mask physical features, including instability signatures and SEE effects, thereby affecting the fidelity of thruster performance predictions [19]. Improving interpolation accuracy and robustness is therefore critical. Moreover, fidelity in PIC simulations directly impacts design life and durability assessments. In HET, energetic ions sputter the discharge channel walls, causing erosion that limits lifetime [22]. Because direct long-duration testing is costly and measurements are constrained, enhanced numerical models are needed to reliably predict erosion, guide geometry refinement, and inform

the selection of erosion-resistant materials and coatings [23]. This dictates constraints to fast and accurate PIC simulations.

This work addresses these challenges through a comparative study of interpolation schemes for the Particle-Mesh step, with special emphasis on a modified cubic B-Spline kernel that introduces small, zero-mean random perturbations around the standard kernel shape. The rationale is twofold: (i) to emulate unresolved micro-scale fluctuations that are otherwise smoothed by deterministic kernels, and (ii) to mitigate spurious ringing and cell-to-cell oscillations arising from superparticle clustering. We compare three interpolation families: classical trilinear (CIC), standard cubic B-Spline, and modified cubic B-Spline [22]. The modified cubic B-Spline is tested in serial and OpenMP-parallel implementations to assess not only physical accuracy and stability but also computational performance and scalability.

To ensure a controlled, repeatable setting for verification, we use the cubic electrostatic benchmark described by Brieda [23]. The domain is a grounded cubic box with equal initial number densities for electrons and ions; one octant is initialized with electrons while the remaining volume is filled with ions. This configuration produces an imbalance in electric forces that drives electron-ion dynamics and exposes Particle-Mesh interpolation errors. Our evaluation metrics include charge-conservation error, the electric field, and parallel performance (throughput and strong-scaling efficiency). The OpenMP design parallelizes the charge-assignment, field-interpolation, and particle-push loops while preserving determinism via seedable per-thread random streams for the modified kernel.

Contributions. (i) We evaluate a modified cubic B-Spline interpolation that suppresses mesh-scale oscillations and noise relative to CIC and standard cubic kernels. (ii) We present an OpenMP-parallel implementation that maintains the accuracy benefits of the modified kernel with marginal overhead and strong scalability (in time). (iii) We provide a systematic, apples-to-apples comparison on a controlled 3D benchmark, reporting accuracy, stability, and performance metrics relevant to nonlinear electron-ion PIC.

2. Governing equations and the Particle-Mesh step

The Vlasov equations (1) describe the transport of the distribution function (DF) assuming no collisions; for ions, $f_i(r_j, u_j, t)$, and electrons, $f_e(r_j, u_j, t)$, respectively; r_j is the position vector, u_j velocity vector, and t time, for $j = 1, 2, 3$. The Eq. (2) models the change in electric potential ϕ as a function of the charge density ρ and the permittivity of free space ϵ_0. In this way, the charge density is obtained by the sum of the integration DF in the momentum space for each species [10].

$$\frac{\partial f_i}{\partial t} + v_j \frac{\partial f_i}{\partial r_j} + \frac{q_i}{m_i}(E_j + \epsilon_{jkl} v_k B_l)\frac{\partial f_i}{\partial vj} = 0,$$

$$\frac{\partial f_e}{\partial t} + v_j \frac{\partial f_e}{\partial r_j} + \frac{q_e}{m_e}(E_j + \epsilon_{jkl} v_k B_l)\frac{\partial f_e}{\partial v_j} = 0, \quad (1)$$

$$\frac{\partial^2 \phi}{\partial r_j^2} = -\frac{\rho}{\epsilon_0}. \quad (2)$$

According to [25], we can rewrite Eq. (1) as the transport equation for the DF as

$$\frac{\partial \mathbf{q}}{\partial t} + \mathbb{A}\mathbf{q} = 0, \quad (3)$$

where $\mathbb{A}$ is a differential operator that can be decomposed into $\mathbb{A} = \mathbb{E} + \mathbb{L}$. Using the splitting scheme, the Eq. (3) can be decomposed into two auxiliary problems.

$$\frac{\partial \overline{\mathbf{q}}}{\partial t} + \mathbb{E}\overline{\mathbf{q}} = 0, \quad (4)$$

$$\frac{\partial \mathbf{q}}{\partial t} + \mathbb{L}\mathbf{q} = 0, \quad (5)$$

t_p is a particular time, τ is a time step.

Discretizing the domain $\Omega_{rv} = \Omega \setminus \mathbb{R}^1_+$ in cells denoted as $\{\omega_\alpha\}$; we will arrive at

$$\Omega_{rv} = \bigcup_\gamma (\{\omega_\alpha \cup \omega_\beta\})_\gamma. \quad (6)$$

We have two auxiliary problems that describe Eqs. (3), (4) refers to the space domain, commonly called the *Eulerian step*; and Eq. (5) is called the *Lagrangian step*. To construct the solution of Eq. (4) we use the elements that represent the space domain, since the description of the variable, $\overline{\mathbf{q}}$, is a function of the actual step time.

Equation (5) must be solved for the $t_p + \tau$ time. If the operator $\mathbb{L}$ represents the phase-space gradient of the function $\mathbf{q}$,

$$\mathbb{L}\mathbf{q} = \frac{\partial \mathbf{U}\mathbf{q}}{\partial \mathbf{r}} + \frac{\partial \mathbf{U}\mathbf{q}}{\partial \mathbf{v}} = \frac{\mathbf{U}\mathbf{q}}{\partial \mathbf{u}}, \quad (7)$$

$\mathbf{u} \in \Omega_{ru}$. Rewriting Eq. (5) using Eq. (7)

$$\frac{\partial \mathbf{q}}{\partial t} + \frac{\partial \mathbf{U}\mathbf{q}}{\partial \mathbf{u}} = 0. \quad (8)$$

Here $\mathbf{U} = \mathbf{U}(\mathbf{u}, t)$ is the *transport of the property* $\mathbf{q}$. Integrating (8)

$$\int_{\Omega_{ru}} \left(\frac{\partial \mathbf{q}}{\partial t} + \frac{\partial \mathbf{U}\mathbf{q}}{\partial \mathbf{u}} \right) = 0. \quad (9)$$

Applying the Gauss theorem and note $\mathbf{Q} = \int_{\Omega_{ru}} \mathbf{q} d\mathbf{u}$, we arrive at

$$\frac{\partial \mathbf{Q}}{\partial t} + \int_{\partial\Omega_{ru}} (\mathbf{n} \cdot \mathbf{U}\mathbf{q}) d\partial\Omega_{ru} = 0, \quad (10)$$

$\mathbf{n}$ is the normal vector pointing outward to the boundary $\partial\Omega_{ru}$.

Proposing the solution of Eq. (10) as

$$\mathbf{q}(\mathbf{u},t)=\sum_{i=1}^{N}\mathbf{Q}_i R(\mathbf{u},\mathbf{u}_i). \tag{11}$$

This solution, Eq. (11), represents the discretization of $\mathbf{u}$ into *superparticles*. The vector $\mathbf{Q}_i$ represents the set of features carried by the i-superparticle, this vector is not a function of time. The function $R(\mathbf{u},\mathbf{u}_i)$ is the interpolation shape of the superparticle, called the kernel. Due to the fact that the vector Q_i is time-independent, it must be satisfied.

$$\mathbf{Q}=\sum_{i=1}^{N}\mathbf{Q}_i. \tag{12}$$

Introducing the weak formulation for (5) using the procedure employed by [28],

$$\int_{\Omega_{ru}}\phi(\mathbf{u})\left(\frac{\partial \mathbf{q}}{\partial t}+\frac{\partial \mathbf{qU}}{\partial \mathbf{u}}\right)d\mathbf{u}=0, \tag{13}$$

where $\phi(\mathbf{u})$ is an arbitrary smooth test function. Using Eq. (11) in (13)

$$\int_{\Omega_{ru}}\phi(\mathbf{u})\Bigg(\frac{\partial}{\partial t}\sum_{i=1}^{N}\mathbf{Q}_i\,R(\mathbf{u},\mathbf{u}_i) + \frac{\partial}{\partial \mathbf{u}}\sum_{i=1}^{N}\mathbf{Q}_i\,R(\mathbf{u},\mathbf{u}_i)\,\mathbf{U}\Bigg)\,\mathrm{d}\mathbf{u}=0. \tag{14}$$

Using $R(\mathbf{u},\mathbf{u}_i)=R$, and making a mathematical treatment,

$$\sum_{i=1}^{N}\mathbf{Q}_i\int_{\Omega_{ru}}\phi(\mathbf{u})\left(\frac{\partial R}{\partial t}+\frac{\partial R(\mathbf{u},\mathbf{u}_i)\mathbf{U}}{\partial \mathbf{u}}\right)d\mathbf{u}=0, \tag{15}$$

$$\int_{\Omega_{ru}}\left(\frac{\partial R}{\partial \mathbf{u}_j}\frac{d\mathbf{u}_j}{dt}\phi+R\mathbf{U}\frac{\partial \phi}{\partial \mathbf{u}}\right)d\mathbf{u}=0. \tag{16}$$

If we make a change of variable $\mathbf{u}\leftrightarrow\mathbf{u}_j$

$$\int_{\Omega_{ru}}R\frac{\partial\phi}{\partial \mathbf{u}_j}\left[\frac{d\mathbf{u}_j}{dt}-\mathbf{U}(\mathbf{u}_j)\right]d\mathbf{u}_j=0. \tag{17}$$

Due to the arbitrariness of the test function, the Eq. (17) must satisfy the condition

$$\frac{d\mathbf{u}_j}{dt}=\mathbf{U}(\mathbf{u}_j). \tag{18}$$

The Eq. (18) is a generalized result for the problem (8), relating the evolution of variable $\mathbf{u}_j$ for the j-th particle with some j-th transport property of the solution q.

To describe the transport property we perform the same procedure used in Eq. (8), but with the expression of the operator $\mathbb{L}$ in terms of the two subspaces of the domain, Eq. (7). In this way, Eq. (8) will have the same shape as Eq. (1).

If we assume the solution of the Eq. (1) as

$$f_s(\mathbf{r},\mathbf{v},t)=\sum_{j=1}^{N}\mathbf{Q}_j R(\mathbf{r},\mathbf{r}_j)R(\mathbf{v},\mathbf{v}_j), \tag{19}$$

subscript s refers to the s-th species, assuming that the kernel in the velocity-space is the Dirac delta function, we rewrite Eq. (19)

$$f_s(\mathbf{r},\mathbf{v},t)=\sum_{j=1}^{N}\mathbf{Q}_j R(\mathbf{r},\mathbf{r}_j)\delta(\mathbf{v}-\mathbf{v}_j). \tag{20}$$

The kernel $R(\mathbf{r},\mathbf{r}_j)$ in Eq. (19) has the same properties as the kernel in Eq. (11), that is $\int_{\Omega_r}R(\mathbf{r},\mathbf{r}_j)d\mathbf{u}=1$ and $R(\mathbf{r},\mathbf{r}_j)=R(\mathbf{r}_j,\mathbf{r})\geq 0$.

As we mentioned, assuming an electrostatic phenomenon, multiplying the Eq. (1) by some arbitrary smooth test function $\phi(\mathbf{r},\mathbf{u}_j)$ and performing an integration in the position-space,

$$\int_{\Omega_r}\phi(\mathbf{r},\mathbf{u}_j)\left[\frac{\partial f_s}{\partial t}+v_j\frac{\partial f_s}{\partial r_j}+\frac{q_sE_j}{m_s}\frac{\partial f_s}{\partial v_j}\right]d\mathbf{r}=0. \tag{21}$$

Using the solution from Eq. (20) in Eq. (21) and rearranging

$$\sum_{j=1}^{N}\mathbf{Q}_j\Bigg\{\int_{\Omega_r}\Bigg[\frac{\partial}{\partial t}(\phi R) + v_j\frac{\partial}{\partial r_j}(\phi R)-\frac{q_sE_j}{m_s}R\frac{\partial\phi}{\partial v_j}\Bigg]\mathrm{d}r_j\Bigg\}=0. \tag{22}$$

Making a differentiation in time, integrating by parts and regrouping, Eq. (22) will be

$$\sum_{j=1}^{N}\mathbf{Q}_j\Bigg\{\int_{\Omega_r}\left[(\dot{r}_j-v_j)\frac{\partial\phi}{\partial r_j}\right]\mathrm{d}r_j \tag{23}$$

$$+\int_{\Omega_r}\left[\left(\dot{u}_j-\tfrac{q_sE_j}{m_s}\right)R\frac{\partial\phi}{\partial v_j}\right]\mathrm{d}r_j\Bigg\}=0. \tag{24}$$

Making a change of variable, similar to Eq. (17), but using $\mathbf{r}\leftrightarrow\mathbf{r}_j$ and because of the arbitrariness of the test function $\phi(\mathbf{r},\mathbf{v})$, we arrive at the following.

$$\begin{aligned}\frac{dr_j}{dt}&=v_j,\\ \frac{dv_j}{dt}&=\frac{q_s\overline{E}_j}{m_s}.\end{aligned} \tag{25}$$

Here, the term $\overline{E}_j$ is the generalized electric force field acting on the modeled particle with the multiplication of the kernel R. In this sense, the generalized electric force field is obtained by

$$\overline{E}_j=\int_{\Omega_r}E_jRdr_j. \tag{26}$$

Due to the properties of the kernel, we guaranty the non-negativity and normalization in Eq. (26), as well as the deterministic averaging with respect to the distribution of the kernel.

As we can see, the kernel plays a key role in obtaining the velocity of the modeled particle.

After the Lagrangian step, and before the next step given by τ, we project the solution f_s in the form of Eq. (20) into the space of the mesh functions $\{\tilde{q}_\alpha\}$. For the calculation of the fields.

For the present study, we compare interpolation methods for the particle-mesh interpolation step: i) Trilinear interpolation, $T(r)$, ii) Third-order B-spline interpolation, $S^3(\mathbf{r})$, and iii) Third-order B-spline modified interpolation, $S^3_m(\mathbf{r}_m)$, following the stochastic amplitude-shape perturbation proposed in Ref. [31], in serial and parallel. The third order B-spline modified interpolation is carried out using random number generation with a uniform distribution. The common B-spline, Eq. (27) and the B-spline modified in Eq. (28)

$$S^3(\mathbf{r}) = \begin{cases} \frac{1}{2}|r^3| - r^2 + \frac{2}{3}|r| & |r| \leqslant 1, \\ \frac{4}{3}(1 - \frac{1}{2}|r|)^3 & 1 \leqslant |r| \leqslant 2, \\ 0 & |r| \geqslant 2, \end{cases} \tag{27}$$

$$S^3_m(\mathbf{r}_m) = \gamma_m \begin{cases} \frac{1}{2}|r^3_m| - r^2_m + \frac{2}{3}|r_m| & |r_m| \leqslant 1, \\ \frac{4}{3}(1 - \frac{1}{2}|r_m|)^3 & 1 \leqslant |r_m| \leqslant 2, \\ 0 & |r_m| \geqslant 2. \end{cases} \tag{28}$$

The Eq. (28) shows the modified third-order B-spline, where γ_m is the random amplitude modification, and r_m is the modification shape vector. We define the shape vector as the scale of the vector **r**,

$$r_m = \frac{\mathbf{r}}{\beta_m}. \tag{29}$$

The modification adjusted the amplitude; if we have a value greater than one, the height will increase. On the other hand, if the value is less than one, the height decreases. The above modifications control the amplitude that adjusts the

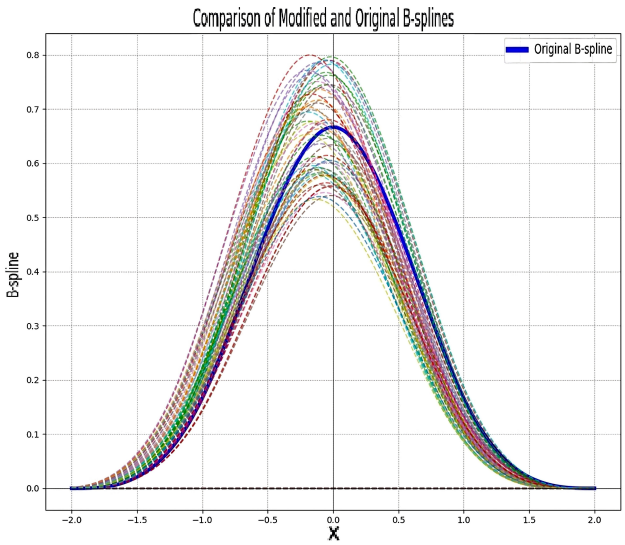

FIGURE 1. Families of modified B-spline and classical B-Spline [31].

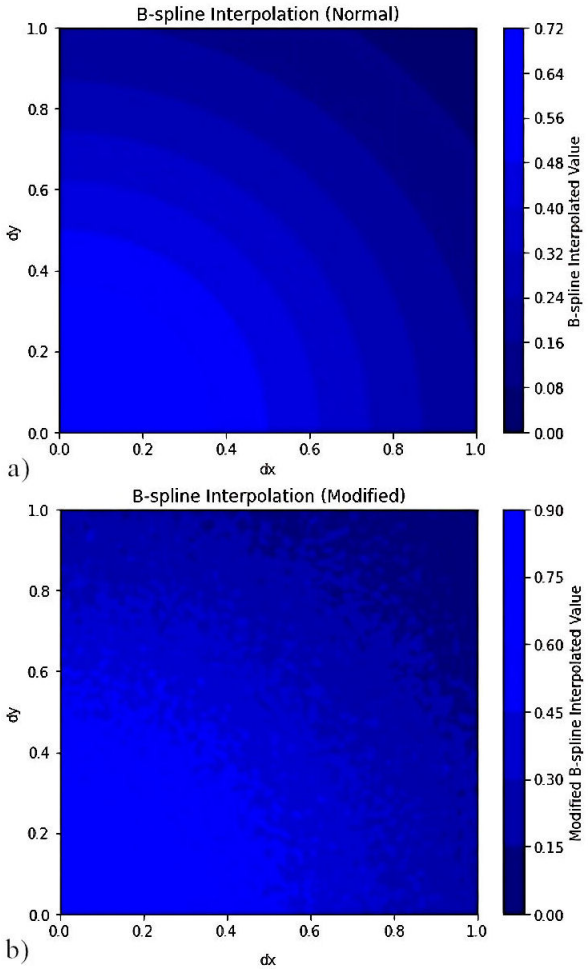

FIGURE 2. Comparative between the common interpolation and modified interpolation. a) B-spline interpolation, and b) Modified B-spline interpolation [31].

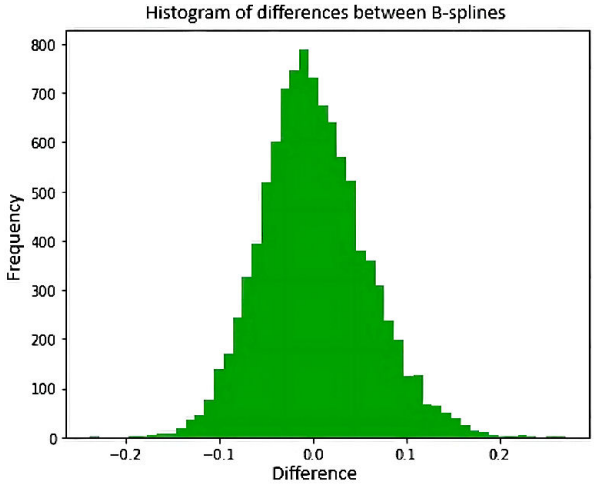

FIGURE 3. Histogram of the frequencies for B-spline interpolation [31].

magnitude by which a particle affects close nodes; and the shape determines how many adjacent nodes will be affected.

Figure 1 depicts the modified interpolation that introduces stochastic variability. In Figs. 2 and 3 we have a smoother distribution and small differences that suggest a smaller impact on the noise. This interpolation method preserves the physical properties, so it is less probable to introduce significant errors in energy and charge conservation. This suggests their applicability in the PIC, introducing variability and describing the stochastic behaviour inherent in the particles.

We perform a statistical analysis to guaranty the properties of B-splines with random modifications; we propose a population of $50,000$ S_m^3. As shown in Fig. 1, the compact support is maintained as well as positivity. On average, the normalization has an integral value of 1.014, so we can assume the normalization property. Applying an L_2 norm to measure the distance from the curve to the y-axis, we guaranty symmetry, finding that 39% of the B-splines do not have symmetry, and the average L_2 norm is 3.804, which indicates significant asymmetry. However, the structure and smoothness remain. This is acceptable because our intention is to introduce asymmetries in the particles.

3. Numerical setup and benchmark

To compare the results of the proposed method, we use the results from the trilinear interpolation used in the problem depicted by Brieda [24]. In this way, we introduce a comparison between trilinear interpolation, B-spline interpolation, and modified B-spline interpolation, serial and parallel. Also, we make a variation in the initial real number of density for four cases: $n = 1e9$, $n = 4.5e9$, $n = 1e10$, $n = 1e11$, and $n = 1e13$.

The configuration of the simulation is a cubic domain with an extent of 0.2 m on each side, divided into a uniform Cartesian mesh with $\triangle\ r = 2.5 \times 10^{-3}$ m. One octant of the domain is filled with computational particles of electrons, with a number density equal to n_e, and the rest of the domain

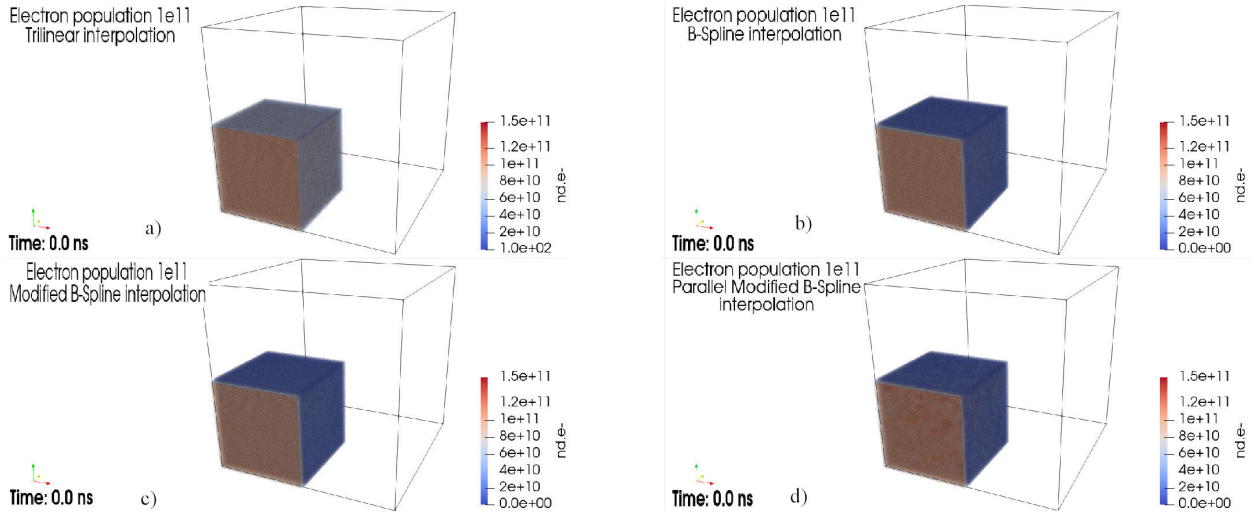

FIGURE 4. Initial conditions for a number of density $n = 1e11$.

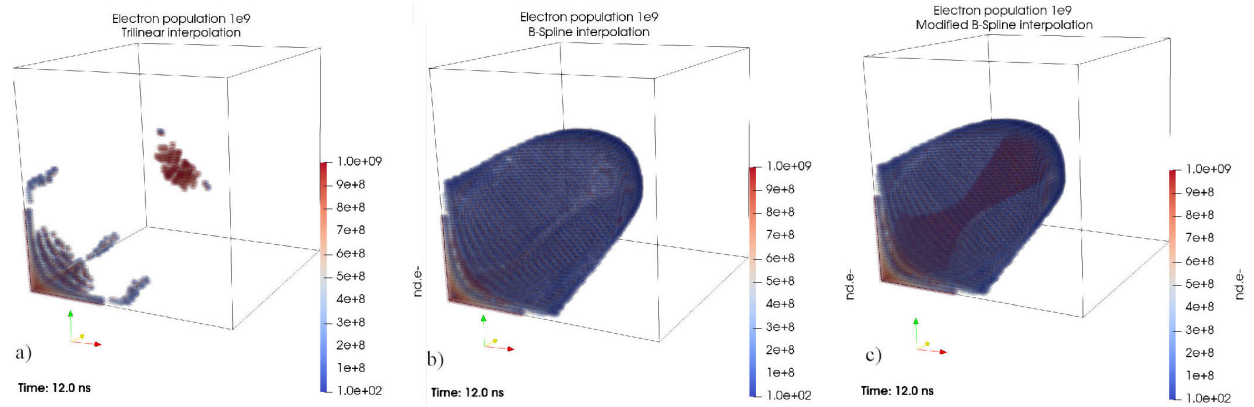

FIGURE 5. Last time for a number of density $n = 1e9$.

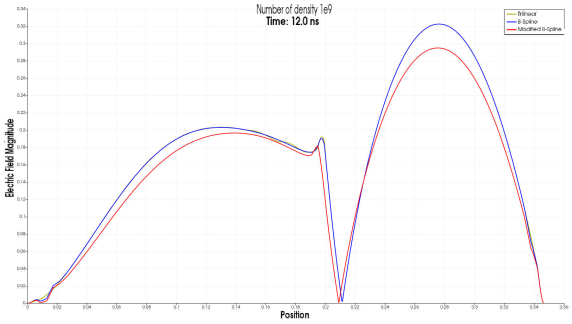

FIGURE 6. Last time for a electric field magnitude over a transversal line, $n = 1e9$.

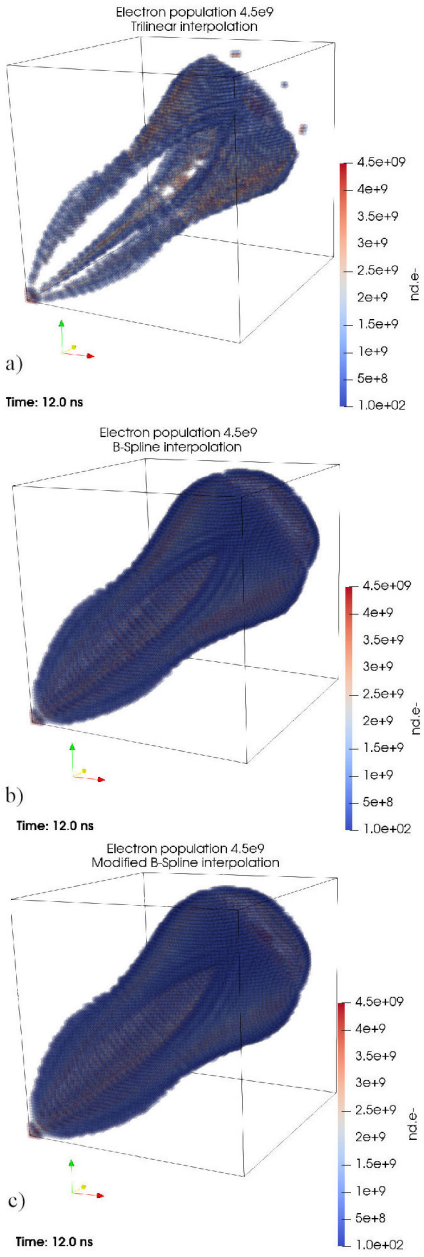

FIGURE 7. Last time for a number of density $n = 4.5e9$.

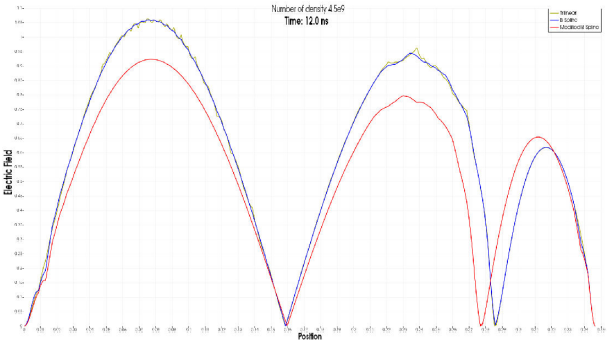

FIGURE 8. Last time for a electric field magnitude over a transversal line, $n = 4.5e9$.

is filled with ions of the same density. In Fig. 4, we can see the initial configuration of the simulation. The time domain is $t \in [0, 12e-9]$, divided into intervals of $\triangle\, t = 1e-10$ s.

Performing an analysis of the problem using a lower number density, we observe that the novel method takes advantage when the number density is greater than $1e10$ particles, so we briefly discuss the behavior of the system for particles less than $1e10$ using only serial methods.

Figure 5 depicts the improvements between the B-Spline methods; the trilinear interpolation shown in Fig. 5a) does not display the same structures that the B-Spline interpolation does; it shows higher dispersions and masks the central structure where the B-Spline and modified B-Spline indicate a central concentration of particles. A plot over a line between a domain vertex in the octant and the opposite vertex of the electric field is depicted in Fig. 6; for the three methods, the results are close.

For a higher number density, the same mask effect of the trilinear interpolation hides the central structure and creates dispersion performance in the distribution of particles. The electric field over a line in Fig. 8 shows differences between the three interpolation methods; we observe higher oscillations in the trilinear interpolation and a close performance of the B-Spline and modified B-Spline.

This short analysis shows certain advantages of the modified method with respect to the classic methods, although it does not demonstrate better performance.

4. Results

The four tests are performed under the same conditions as Figs. 4. We observe that the novel method takes advantage when the number density is higher than $1e10$. Figures 9, 10 and 11 depict the system over three different times; for the trilinear interpolation, we observe a dispersion of the electrons and simplifications of the distribution. The B-spline shows an improvement with respect to trilinear interpolation; the modified B-spline constructs a complex topology of the electron distribution and lower dispersion. With the parallel B-spline interpolations, we observe higher dispersion; however, the structure, in comparison with the B-spline and modified B-spline, is conserved.

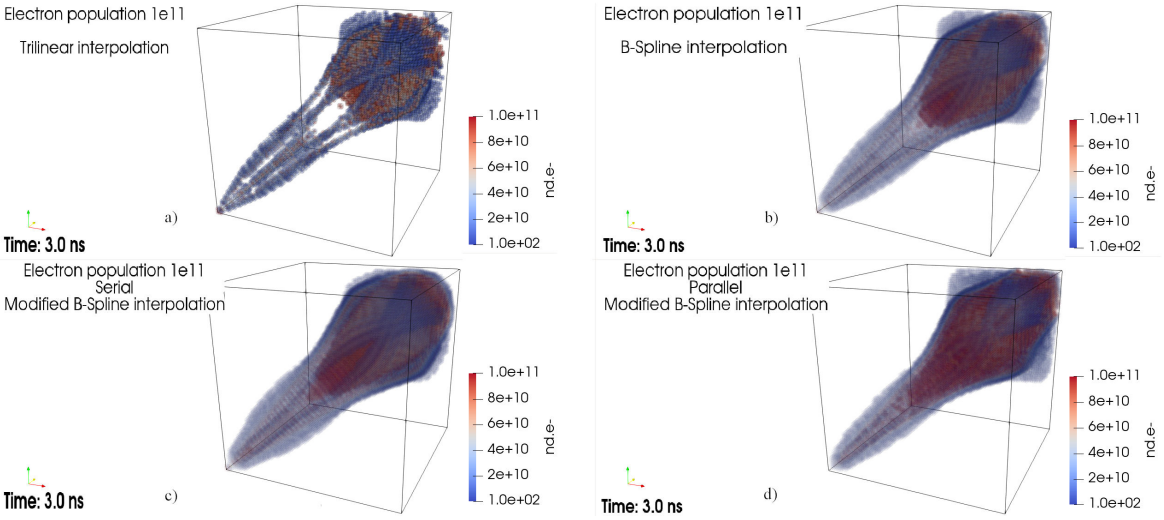

FIGURE 9. Comparative at time $t = 3$ ns between a) trilinear; b) B-Spline; c) Serial Modified B-Spline; d) Parallel Modified B-Spline.

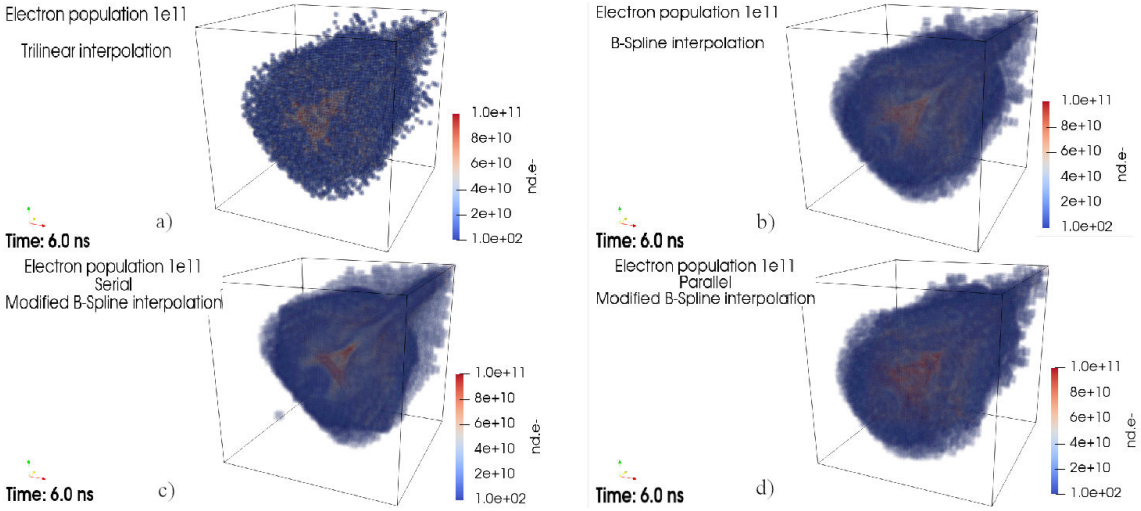

FIGURE 10. Comparative at time $t = 6$ ns between a) trilinear; b) B-Spline; c) Serial Modified B-Spline; d) Parallel Modified B-Spline.

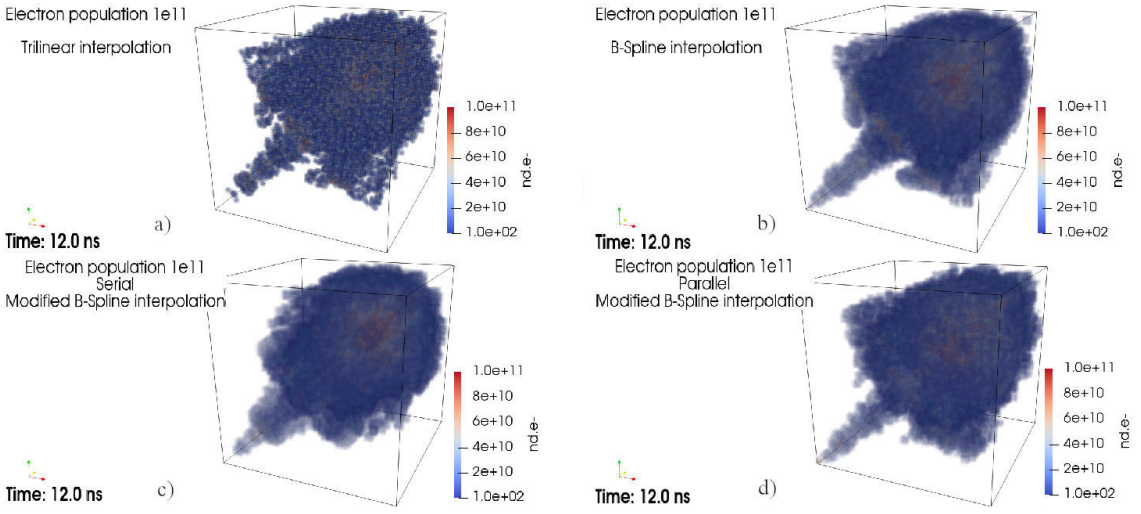

FIGURE 11. Comparative at time $t = 12$ ns between a) trilinear; b) B-Spline; c) Serial Modified B-Spline; d) Parallel Modified B-Spline.

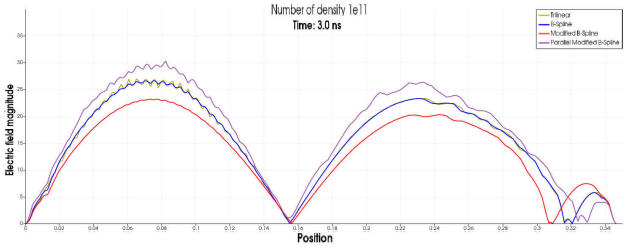

FIGURE 12. Electric field magnitude comparison for time $t = 3$ ns.

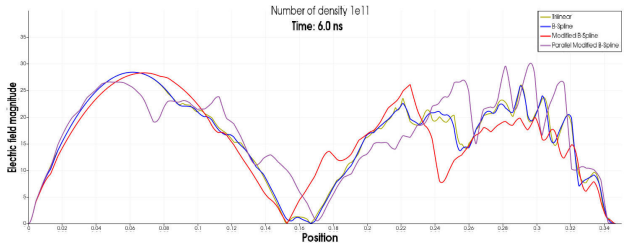

FIGURE 13. Electric field magnitude comparison for time $t = 6$ ns.

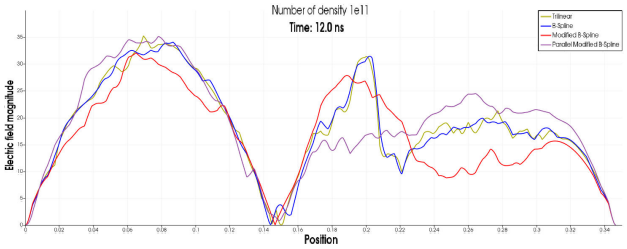

FIGURE 14. Electric field magnitude comparison for time $t = 12$ ns.

Figures 12, 13 and 14 compare the electric field magnitude distribution over a line; it is clear that the plots of the three methods differ in the electric field but maintain the same mean shape. The method with lower oscillation is the serial modified B-spline method; it is the most stable. The trilinear and B-spline interpolations exhibit oscillations during the initial time period. The parallel modified B-spline exhibits oscillations but preserves the shape of the other methods; however, it is clear that it overestimates the magnitude.

The most likely cause is numerical in parallel implementation: (i) in floating-point arithmetic, additions are not associative, so the reordering inherent in parallel reductions/accumulations can introduce small differences in the charge deposited on the mesh and, consequently, in the potential and its gradient; (ii) The modified kernel incorporates stochastic perturbations of amplitude and shape, Eqs. (28) and (29), so that changes in the distribution of the workload by subprocesses and in the order of evaluation can alter the effective sampling of these disturbances. In addition, a local seed per thread was used, inducing variations in the local gradients and amplifying the magnitude of E.

We interpret the overestimation as a numerical reproducibility effect associated with multi-threaded execution (reduction order and stochastic sampling) and not as a modification of the physical model. Future work will explore deterministic reduction (*e.g.*, per-thread accumulators with ordered merging or compensated sum techniques) and/or per-particle deterministic randomness strategies to minimize dependence on the number of threads.

5. Conclusions

We presented a modified cubic B-spline kernel for the Particle-Mesh step of PIC that injects small, zero-mean stochastic perturbations to emulate unresolved microscale variability while preserving compact support and positivity. Across a controlled $3D$ electrostatic benchmark, the modified kernel systematically reduced electric-field oscillations along diagnostic lines relative to CIC and the standard cubic B-spline, without degrading charge conservation or the overall energy behavior, as shown in Fig. 15. Visual diagnostics revealed that Could-in-Cell (trilinear) tends to smear and under-resolve central structures, whereas both cubic kernels

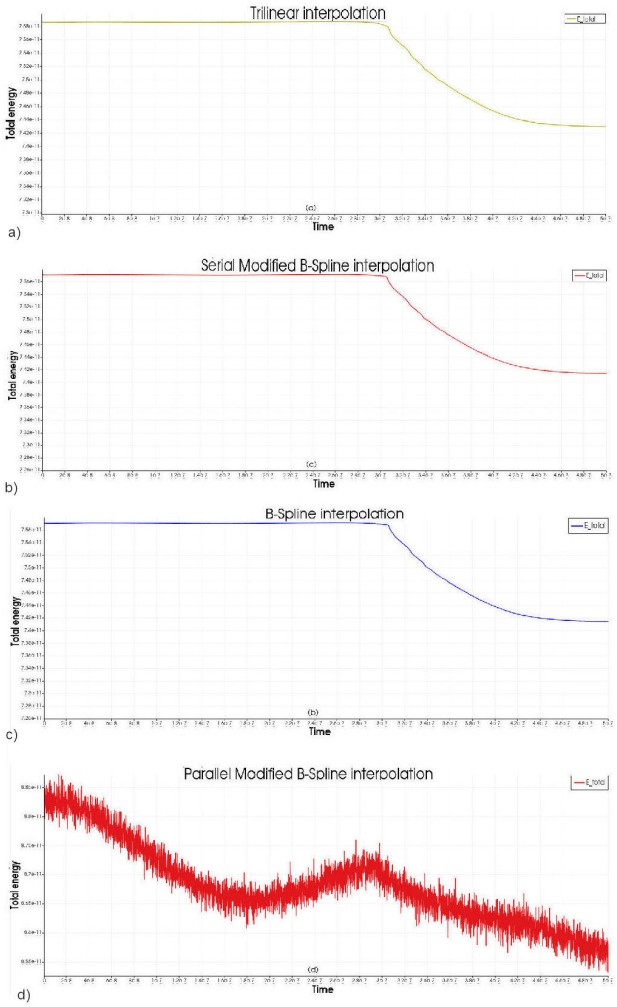

FIGURE 15. Total energy behaviour over time.

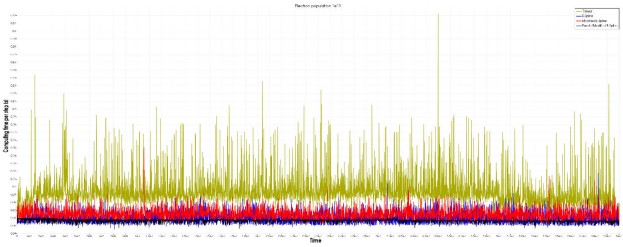

FIGURE 16. Wall-clock time per iteration.

better preserve topology; the modified B-spline further attenuates mesh-scale ringing and superparticle-clustering phenomena. The implementation of the code in OpenMP retained these accuracy benefits with marginal overhead, exhibiting good strong-scaling on shared-memory hardware, Fig. 16. From an application standpoint, the accuracy-robustness-cost trade-off of the modified kernel makes it attractive for high-fidelity electron-ion PIC in Hall effect thruster studies, where reliable electric field statistics, stability signatures, and wall interaction predictions are critical. Limitations and future work. First, while the stochastic perturbations reduce oscillations, they introduce an additional variance source whose bounds must be reported (amplitude and shape scaling), we suggest generating simulations with a larger population $n > 1e11$, something statistically developed and closer to reality. Second, our tests focused on electrostatic, collisionless cases on Cartesian grids; extensions to magnetized, collisional, and curvilinear or unstructured meshes remain to be quantified. Third, the OpenMP implementation targets shared-memory nodes; distributed-memory (MPI) and GPU back ends, as well as mixed-precision strategies, are natural next steps.

1. M. Reza, F. Faraji, and A. Knoll, Plasma dynamics and electron transport in a Hall-thruster-representative configuration with various propellants: I. Variations with discharge voltage and current density, *Plasma* **7** (2024) 651–679, https://doi.org/10.3390/plasma7030034.
2. G. Gallo *et al.*, Numerical aspects of particle-in-cell simulations for plasma-motion modeling of electric thrusters, *Aerospace* **8** (2021) 138, https://doi.org/10.3390/aerospace8050138.
3. I. D. Kaganovich *et al.*, Physics of $E \times B$ discharges relevant to plasma propulsion and similar technologies, *Physics of Plasmas* **27** (2020), https://doi.org/10.1063/5.0010135.
4. R. Sentis, Mathematical Models and Methods for Plasma Physics. Volume 1: Fluid Models (Birkhäuser, Cham, 2016).
5. Rozhansky, Plasma Theory: An Advanced Guide for Graduate Students (Springer, Cham, 2023), https://doi.org/10.1007/978-3-031-44486-9.
6. N. P. Pai, V. S. Sampath Kumar, B. Devaki, and G. Bhat Pareekshith, Analysis of heat and mass transfer in MHD laminar fluid flow between parallel plates of different permeability, *Cogent Engineering* **11** (2024), https://doi.org/10.1080/23311916.2024.2430437.
7. D. V. Kolasseril and D. C. Joshi, Numerical simulation of MHD flow over a shrinking sheet using finite element B-spline collocation technique, *International Journal for Computational Methods in Engineering Science and Mechanics* **13** (2012) 392–402, https://doi.org/10.1080/15502287.2012.698709.
8. A. V. Bobylev, Kinetic Equations. Volume 1: Boltzmann Equation, Maxwell Models (De Gruyter, Berlin, 2020).
9. D. G. Swanson, Plasma Kinetic Theory (CRC Press, Boca Raton, FL, 2008).
10. G. Colonna and A. D'Angola, eds., Plasma Modeling: Methods and Applications, 2nd ed. (IOP Publishing, Bristol, 2022).
11. B. Srinivasan, W. Scales, P. Cagas, and C. Glesner, Recent advances in plasma modeling for space applications, *Radiation Effects and Defects in Solids* **172** (2017) 74–80, https://doi.org/10.1080/10420150.2017.1286659.
12. F. Filbet, E. Sonnendrücker, and P. Bertrand, Conservative numerical schemes for the Vlasov equation, *Journal of Computational Physics* **172** (2001) 166–187, https://doi.org/10.1006/jcph.2001.6818.
13. C. K. Birdsall and A. B. Langdon, Plasma Physics via Computer Simulation (Taylor & Francis, New York, 2004).
14. J. A. García Pérez and K. Suzuki, Development of object-oriented PIC code for simulation of plasma flow around a satellite in solar corona, *International Journal of Computational Fluid Dynamics* **35** (2021) 685–706, https://doi.org/10.1080/10618562.2022.2026339.
15. G. Lapenta, Particle rezoning for multidimensional kinetic particle-in-cell simulations, *Journal of Computational Physics* **181** (2002) 317–337, https://doi.org/10.1006/jcph.2002.7126.
16. L. Vialetto, H. Sugawara, and S. Longo, Particle propagation and electron transport in gases, *Plasma* **7** (2024) 121–145, https://doi.org/10.3390/plasma7010009.
17. M.-C. Lo, C.-Y. Pan, and J.-S. Wu, On an axisymmetric direct simulation Monte Carlo method, *International Journal of Computational Fluid Dynamics* **35** (2021) 373–387, https://doi.org/10.1080/10618562.2021.1955867.
18. P. Coche and L. Garrigues, A two-dimensional (azimuthal–axial) particle-in-cell model of a Hall thruster, *Physics of Plasmas* **21** (2014), https://doi.org/10.1063/1.4864625.
19. M. Touati *et al.*, Kinetic theory of particle-in-cell simulation plasma and the ensemble averaging technique, *Plasma Physics and Controlled Fusion* **64** (2022), https://doi.org/10.1088/1361-6587/ac9016.
20. A. Lopez Ortega and I. G. Mikellides, 2D fluid-PIC simulations of Hall thrusters with self-consistent resolution of the space-

charge regions, *Plasma* **6** (2023) 550–562, https://doi.org/10.3390/plasma6030038.

21. M. Panelli, D. Morfei, B. Milo, F. A. D'Aniello, and F. Battista, Axisymmetric hybrid plasma model for Hall-effect thrusters, *Particles* **4** (2021) 296–324, https://doi.org/10.3390/particles4020026.
22. B. D. Smith, I. D. Boyd, H. Kamhawi, and W. Huang, Hybrid-PIC modeling of a high-voltage, high-specific-impulse Hall thruster, in Proceedings of the 49th AIAA/ASME/SAE/ASEE Joint Propulsion Conference (AIAA, San Jose, CA, 2013).
23. N. P. Brown and M. L. R. Walker, Review of plasma-induced Hall thruster erosion, *Applied Sciences* **10** (2020), https://doi.org/10.3390/app10113775.
24. L. Brieda, Plasma Simulations by Example (CRC Press, Boca Raton, FL, 2019).
25. M. P. Fedoruk, Y. N. Grigorev, and V. A. Vshivkov, Numerical Particle-in-Cell Methods: Theory and Applications (De Gruyter, Berlin/Boston, 2012).
26. S. H. Kang, PIC-DSMC simulation of a Hall thruster plume with charge exchange effects using pdFOAM, *Aerospace* **10** (2023), https://doi.org/10.3390/aerospace10010044.
27. R. Kumar, A. Choudhary, and S. Baskar, Modified cubic B-spline quasi-interpolation numerical scheme for hyperbolic conservation laws, *Applicable Analysis* **99** (2018), https://doi.org/10.1080/00036811.2018.1489961.
28. P. Šolín, Partial Differential Equations and the Finite Element Method (John Wiley & Sons, Hoboken, NJ, 2005), https://doi.org/10.1002/0471764108.
29. A. Vlasov, Many-Particle Theory and Its Application to Plasma (Gordon and Breach, New York, 1961). Originally published in 1950.
30. G. A. Bird, Molecular Gas Dynamics and the Direct Simulation of Gas Flows (Clarendon Press, Oxford, 1994).
31. G. J. Garnica-Castro, G. Polupan, O. M. Huerta-Chavez, and O. Lopez-Perez, Impact of modified B-splines on particle-in-cell modeling for electron-ion nonlinear dynamics, *Cogent Engineering* **12** (2025), https://doi.org/10.1080/23311916.2025.2575106.